



Published in final edited form as:

*J Biomed Opt.* 2008 ; 13(5): 054001. doi:10.1117/1.2981828.

## Confocal mosaicing microscopy in Mohs skin excisions: feasibility of rapid surgical pathology

**Daniel S. Gareau,**

*Memorial Sloan-Kettering Cancer Center, Dermatology Service, 160 East 53rd Street, New York, New York 10022*

**Yongbiao Li,**

*Memorial Sloan-Kettering Cancer Center, Research Engineering Laboratory, 1275 York Avenue, New York, New York 10021*

**Billy Huang,**

*Bronx High School of Science, 75 West 205th Street, Bronx, New York 10468*

**Zach Eastman,**

*Lucid Inc., 2320 Brighton Henrietta T/L Road, Rochester, New York 14623*

**Kishwer S. Nehal, and**

*Memorial Sloan-Kettering Cancer Center, Dermatology Service, 160 East 53rd Street, New York, New York 10022*

**Milind Rajadhyaksha**

*Memorial Sloan-Kettering Cancer Center, Dermatology Service, 160 East 53rd Street, New York, New York 10022*

### Abstract

Mosaicing of confocal images enables observation of nuclear morphology in large areas of tissue. An application of interest is rapid detection of basal cell carcinomas (BCCs) in skin excisions during Mohs surgery. A mosaic is currently created in less than 9 min, whereas preparing frozen histology requires 20 to 45 min for an excision. In reflectance mosaics, using acetic acid as a contrast agent to brighten nuclei, large and densely nucleated BCC tumors were detectable in fields of view of 12 × 12 mm (which is equivalent to a 2×-magnified view as required by Mohs surgeons). However, small and sparsely nucleated tumors remained undetectable. Their diminutive size within the large field of view resulted in weak light backscatter and contrast relative to the bright surrounding normal dermis. In fluorescence, a nuclear-specific contrast agent may be used and light emission collected specifically from nuclei but almost none from the dermis. Acridine orange of concentration 1 mM stains nuclei in 20 s with high specificity and strongly enhances nuclear-to-dermis contrast of BCCs. Comparison of fluorescence mosaics to histology shows that both large and small tumors are detectable. The results demonstrate the feasibility of confocal mosaicing microscopy toward rapid surgical pathology to potentially expedite and guide surgery.

### Keywords

confocal microscopy; mosaicing; surgical pathology; basal cell carcinomas (BCCs); Mohs surgery; acridine orange

## 1 Introduction

Precise surgery of tumor with minimal damage to the surrounding normal tissue is achieved with a series of excisions that are guided by frozen histology. Examples include Mohs surgery for the removal of basal cell carcinomas (BCCs) in skin, excisions of oral mucosal lesions, thyroid nodules, parathyroid glands and bone during head-and-neck surgery, needle core-biopsies and lumpectomies of breast, and intraoperative biopsies of liver, bladder, and many other tissues.

Mohs surgery typically requires from two to several excisions. Frozen histology sections are prepared of each excision during surgery. Examination for the presence and location of tumor in the histology sections of each excision guides the subsequent excision. The preparation of frozen histology sections is labor-intensive and slow such that Mohs surgery usually lasts from two to several hours.<sup>1</sup> Approximately 1 million Mohs surgeries are performed per year in the United States, with total treatment costs of approximately \$1 billion.<sup>2</sup> The costs for conventional frozen histology is ~15%, which amounts to \$150 million per year. Worldwide, too, the incidence of BCCs is growing, with associated increase in treatment costs.

Confocal mosaicing microscopy offers an attractive alternative to frozen histology since nuclear morphology may be imaged in real time and directly in freshly excised tissue<sup>1,3,4</sup> Images may be stitched together to create mosaics to display large areas of tissue, as necessary for surgical pathology. Recently, we demonstrated the ability to create mosaics that display up to 12 × 12 mm of tissue in Mohs surgical excisions.<sup>4</sup> The large field of view of 12 × 12 mm corresponds to a view with 2× magnification that is routinely used by Mohs surgeons when examining frozen histology with a standard light microscope. Mosaics were created in less than 9 min, whereas preparation of frozen histology requires 20 to 45 min per excision.<sup>1,4</sup> Thus, large-area mosaicing may offer a means for rapid examination of BCCs directly in fresh excisions while minimizing labor and costs. Confocal mosaicing microscopy may evolve into an adjunct or, perhaps, an entirely new alternative to frozen histology. The technology may enable rapid surgical pathology-at-the-bedside to potentially expedite and guide surgery in skin and other tissues.

In previous work, acetic acid was used as a contrast agent to “aceto-whiten” or brighten nuclei in reflectance.<sup>1,3,4</sup> However, the strongly scattering surrounding normal dermis appeared bright, too. Consequently, large and densely nucleated tumors as in superficial and nodular BCCs were easily detected in mosaiced fields of view of 12 × 12 mm. Small, including especially tiny strands, and sparsely nucleated tumors as in micronodular, infiltrative, and sclerosing BCCs were not.

Small nodules and tiny strands of tumors may contain as few as 5 to 10 nuclei. These are easily seen in individual confocal images that display small fields of view with high magnification. However, the small tumors “disappear” and are not seen in mosaics that display large fields of view with low magnification. The detected power and therefore the perceived contrast and visual detectability of a tumor (or any feature) depend on size relative to the surrounding background. A nucleus in a BCC tumor is typically seen as ~100 pixels in an individual image but subsequently appears as only ~1 pixel in a mosaic. This is due to scaling down of full-resolution mosaics by ~10× to match the pixelation and resolution to that of a 2× view of histology, as explained in an earlier paper.<sup>4</sup> Using a Mie-scattering model for detectability in a reflectance confocal microscope,<sup>5</sup> the nuclear contrast was calculated to drop from ~100 to ~1 relative to the surrounding bright dermis, resulting in a significant loss of visual detectability of small and tiny BCC tumors.

In fluorescence, however, with a contrast agent that specifically stains nuclei, very little light may be collected from the surrounding dermis (except, perhaps, for weak autofluorescence). Detection of both large and small BCC tumors and also squamous cell carcinomas (SCCs) in fluorescence with methylene blue and toluidene blue was recently reported.<sup>6</sup> We chose acridine orange, which is another well-proven nuclear stain for confocal microscopy. Acridine orange differentially stains nuclear DNA and cytoplasmic RNA in endothelial cells.<sup>7</sup> However, staining was expected to be only of the nucleus in epidermal keratinocytes.<sup>8</sup> Acridine orange has a quantum yield of 75% when bound to DNA<sup>9</sup> and an extinction coefficient of  $\sim 53,000$  L/mole-cm. Using an analytical model for detectability in a fluorescence confocal microscope,<sup>10</sup> the nuclear contrast was estimated to drop from  $10^5$  to  $10^3$  relative to a significantly darkened dermis. Thus, small and tiny tumors were expected to be seen in mosaics.

In this paper, we report on the use of fluorescence with acridine orange to increase the nuclei-to-dermis contrast of BCC tumors in confocal mosaics. Advances in the original tissue fixture and image-stitching algorithm are described that show improvements in the appearance and quality of mosaics. The visual comparison of mosaics to the corresponding Mohs frozen histology is described. The results show that the detectability of small BCC tumors such as micronodular, infiltrative, and sclerosing is considerably improved over that in reflectance. The detectability of both large and small—i.e., all types of—tumors demonstrates the feasibility of large-area confocal mosaicing microscopy toward rapid pathology in surgically excised tissue to potentially expedite and guide surgery.

## 2 Materials and Methods

### 2.1 Preparation and Staining of Mohs Surgical Skin Excisions

Skin excisions from Mohs surgery were obtained from our collaborating Mohs surgeon in the Dermatology Service at Memorial Sloan-Kettering Cancer Center, following approval from our Institutional Review Board. During surgery, each excision is processed by a Mohs technician and 3 to 5 frozen histology sections are prepared, each section being  $\sim 5$  to 6 mm thin. After the Mohs surgeon has examined the frozen sections, the remainder of the excision is discarded. These discarded excisions were collected. Often, triangular-shaped excisions of normal skin are made adjacent to the crater-shaped wound that remains after removal of the tumor. Such excisions are necessary for cosmetically efficient suturing and closing of the wound. These excisions are called “dog-ears” because of their shape. Fresh normal dog-ear skin excisions were also collected soon after they were discarded.

The collected Mohs excisions were frozen in the embedding medium that is used to prepare histology sections. Each excision was thawed, rinsed in isotonic saline solution for 30 s, and placed in a solution of acridine orange (Fluka, 01660) in saline for various times and concentrations. Concentrations of 0.3 mM and 1.0 mM were tested for staining skin excisions by immersing for 5 s, 20 s, 1 min, 3 min, and 5 min. Five excisions were tested for each concentration and time, resulting in a total of 50. After staining, excess dye was rinsed from the dermis by dipping in isotonic saline solution for 2 to 3 s. The excisions were mounted in a custom-designed tissue fixture and imaged with a confocal microscope.

Fifty Mohs surgical excisions of BCCs were imaged in the process of optimizing the staining procedure. The images were visually evaluated, and the minimum time was determined for brightening of nuclei and detectability of BCCs. The evaluation was limited to only the exposed surface of the excisions since the Mohs surgeon mainly needs to determine the lateral spread of tumor on the excised surface. Concentration of 1 mM and immersion time of 20 s was chosen as the optimum for rapid staining and strong fluorescence. After this preliminary feasibility test, for further instrumentation development, excisions were stained with 1 mM acridine

orange for immersion time of 20 s. Subsequently, 50 more excisions were similarly stained and imaged for the clinical comparison-to-histology work.

## 2.2 Diffusion of Contrast Agent into Tissue

Only the excised tissue surface is examined in Mohs histology, to determine the lateral extent of tumor. Thus, for imaging, staining with acridine orange was necessary only superficially through a few cell layers. A cell layer in skin is about ~10  $\mu\text{m}$  thin, and the Mohs surgeon usually examines 3 to 5 frozen histology sections, each being ~5 to 6- $\mu\text{m}$  thin. Hence, we consider imaging to a maximum depth of ~30  $\mu\text{m}$ , which corresponds to ~3 cell layers. (This depth is also approximately the maximum to which real-time confocal imaging is possible in dermal tissue with very low milliwatt power blue 488-nm illumination.)

Rapid staining depends on the diffusion of the fluorescent dye into the excised tissue. The uptake kinetics of any particular dye depends on molecular weight and tissue conditions such as pressure in interstitial spaces.<sup>11</sup> The average time  $t$  (s) for diffusion across a distance  $x$  (cm) may be determined from the diffusion coefficient  $D$  ( $\text{cm}^2/\text{s}$ ) as

$$t = \frac{x^2}{2D}. \quad (1)$$

The diffusion coefficient varies with molecular weight  $M_r$  in tumor and normal tissue<sup>12</sup> by the following power law:

$$D = a(M_r)^b. \quad (2)$$

Experiments by Nugent and Jain<sup>12</sup> determined the coefficients to be  $a=10^6$ ,  $b=-2.96$  for normal tissue, and  $a=2.51 \times 10^{-2}$ ,  $b=-1.14$  for tumor (VX2 carcinoma, rabbit). For acridine orange, the diffusion coefficient is then calculated to be  $15.2 \times 10^{-3}$  ( $\text{cm}^2/\text{s}$ ) in normal tissue and  $24.5 \times 10^{-3}$  ( $\text{cm}^2/\text{s}$ ) in tumor, assuming similar order-of-magnitude parameters for normal skin and BCC tumors. Using  $x=30 \mu\text{m}$  in Eq. (1), the average diffusion time is 0.6 (ms) for tumor and 0.37 (s) for normal tissue.

## 2.3 Confocal Microscope and Tissue Fixture

Figure 1 shows the experimental setup. The confocal microscope was described in detail in our earlier reports on reflectance mosaicing.<sup>1,3,4</sup> Briefly, the original reflectance microscope (VivaScope 2000, Lucid, Inc., Rochester, New York) was modified by incorporating an argon-ion laser for fluorescence excitation at 488 nm and a corresponding fluorescence detection channel. The illumination of tissue, is with low-level power of 0.3 to 1.0 (mW). The fluorescence detection optics consists of a dichroic beamsplitter (Chroma, 510DC-SPRX), an excitation rejection filter (Omega Optical, 510EFLP) to block extraneous reflected light, and an avalanche photodiode (Perkin-Elmer, Quebec, Canada, C30659-900-R8A). Detection in the fluorescence channel was mainly of the emission from the acridine orange-stained nuclei, with almost none from the cytoplasm. Autofluorescence from the dermis is a few orders of magnitude weaker than the fluorescence from acridine orange and hence was not detected for the low illumination power and tightly confocal (i.e., small pinhole) detection conditions.

A custom-designed water immersion objective lens (StableView, Lucid, Inc.) was used for imaging through a 1-mm-thick glass slide. Instead of thin coverslips that are conventionally used with objective lenses, a thick glass slide is necessary for mounting and stabilizing

unconventional tissue specimens such as surgical excisions. The objective lens features 30 $\times$  magnification to provide a 430- $\mu\text{m}$  field of view. With a numerical aperture (NA) of 0.9, the calculated axial section thickness is:  $\Delta z = 1.4 \text{ n}\lambda / \text{NA}^2 = 1.1 \mu\text{m}$  and the lateral resolution is:  $\Delta x = 0.46 \lambda / \text{NA} = 0.25 \mu\text{m}$ , which is adequate for imaging nuclear morphology. As previously explained,<sup>4</sup> water was often substituted with a water-based gel as an immersion medium.

Surgical excisions are often thick, large, and of unusual shape. Furthermore, the tissue is fresh, living, hydrated, and mechanically compliant and hence not easy to mount in a microscope. A custom tissue fixture was engineered for Mohs surgical excisions to be mounted and gently compressed onto a microscope slide. Design details of the original tissue fixture are in an earlier report.<sup>4</sup> The operation requires a threaded piston to be tightened for gently compressing and embedding in a gel disk, so as to stabilize the excision. However, the rotational motion of the piston caused the gel and subsequently the edges of the tissue to twist and distort. Such distortion is now prevented with a design modification that includes placing a thin polycarbonate disk and needle-roller bearings (Part No. 5909K31, McMaster-Carr, Dayton, New Jersey) between the piston and the gel disk. The fixture allows repeatable and accurate control of the flattening, tip, tilt, sag, and stability of the tissue surface to be imaged. The functionality of the tissue fixture mimics the operation of a cryostat, which is the standard equipment for preparing frozen histology sections for Mohs surgery. Imaging in reflectance was used to guide  $z$  distance and tip and tilt adjustments such that the tissue surface was oriented exactly parallel to the focal plane of the objective lens. The process involved translating the mounted excision laterally and adjusting four thumbscrews until the focus moved along the reflective water/tissue interface. This alignment enabled acquisition of images contiguously over large areas of 10 to 20 mm. (Engineering drawings, manufacturing methods, and operation details are available to researchers who may be interested.)

After the excision is mounted in the tissue fixture and properly positioned and oriented, confocal images were acquired. Images were acquired of the surface of the excision. Because of the thawing, staining, and rinsing process, small distortions in the imaged surface were expected due to the compliance of the tissue. Thus, the mosaics were expected to show a close but not an exactly one-to-one correspondence to the frozen sections that were prepared by the Mohs technician during surgery.

## 2.4 Acquisition of Images

The small field of view of the 30 $\times$  objective lens (430  $\mu\text{m}$ ) and the large region of interest ( $\sim$ 10 to 20 mm of excised tissue) necessitated the construction of mosaics. A mosaic to display a large area is created by stitching together a two-dimensional (2-D) matrix of confocal images. Mosaics allow observation of large fields of view without sacrificing resolution. The matrix of images was acquired with a continuous step-and-capture routine while translating the tissue fixture with stepper motors-driven linear XY stages (Hayden, Inc., Stamford, Connecticut). An overlap of 10% was included in the translation step distance to correct for a field curvature-induced artifact in the image, as is further explained later. The overlap also prevents loss of detail at the edges between images. The amount of overlap determines the number of images in the matrix that must be acquired, which then determines the total time of acquisition.

Of the 3 to 5 frozen histology sections that are prepared during surgery, the Mohs surgeon usually examines the first to determine the lateral spread of the tumors on the excised surface. Occasionally, if the quality of the first section is poor or if the determination of tumor margins is not very clear, the Mohs surgeon will examine the remaining sections. Additional sections are sometimes prepared if the Mohs surgeon needs to further examine deeper layers of tissue. For this study, however, images were acquired and mosaics created only of the exposed surface of the discarded excisions. This exposed surface corresponds to the last Mohs frozen section.

(Subsequent comparison of the mosaics to histology was therefore limited to the last frozen section.)

Confocal mosaics can be quickly acquired. For acquisition, a continuous step-and-capture routine requires about 5 min for  $36 \times 36$  images. Transferring and archiving images followed by processing to create a mosaic requires another 4 min on another PC. Thus, total time to create a mosaic is up to 9 min at present.

## 2.5 Calibrations for Illumination Artifacts and Vignetting

At the edges of images, dark bands due to field curvature–induced artifact and illumination falloff due to vignetting were noticeably seen. These were corrected for in the image-stitching algorithm, based on calibration measurements in the confocal microscope.

The Petzval field curvature in the microscope was calculated to be  $\sim 3.8 \mu\text{m}$  and measured to be  $\sim 5 \mu\text{m}$ . When focused at the surface of the excision, field curvature results in tissue being seen in the center but surrounded with an annular ring at the periphery in the image. The ring is due to the overlying glass window and results in an illumination artifact. The artifact appears as bright bands in reflectance but dark bands in fluorescence. By focusing slightly deeper than  $5 \mu\text{m}$  beneath the tissue surface, the artifact was often minimized. As a result of deeper focusing, small mismatches to the frozen section of the surface and small losses in correlation to frozen histology were anticipated. The dark bands were largely eliminated by cropping the 10% overlap between images in the image-stitching algorithm.

To characterize vignetting, the illumination falloff across the field of view was measured with a standard fluorescent target. A drop of acridine orange was compressed between a microscope slide and coverslip, and an axial stack of images was acquired. The images were averaged in depth to determine the vignetting in both  $x$  and  $y$  directions (Fig. 2). The vignetting was corrected for with an inverted-brightness polynomial fit in the image-stitching algorithm.

## 2.6 Calibrations for Angular Misalignments and Lateral Registration

The translation of the linear XY stages must be parallel to the  $x$  and  $y$  directions of the optical raster scan in the confocal microscope. Mosaics of a reflective grating test target were used to calibrate for angular misalignments. Figure 2 shows a mosaic of a reflective grating target (Ronchi ruling with 200 lpi, Edmund Industrial Optics) that demonstrates angular alignment and lateral registration in both  $x$  and  $y$  directions. The mosaic was created by cropping the 10% overlap between images and stitching  $3 \times 3$  images. The grating lines appear continuous to within 5 pixels between images. However, as explained here, full-size mosaics are scaled down by 8 to 10 $\times$  such that the lateral mismatch is within a subpixel and not noticeable in the final display.

## 2.7 Image-Stitching Algorithm

Mosaics were created with MATLAB software (version 7.4, MathWorks, Natick, Massachusetts). The algorithm implements the following steps: cropping of the overlap between images, merging of images into a single composite mosaic, and correction for the residual dark bands between images. The amount of cropping was 10%, as predefined by the stepping distance of the XY-translation stages during the image acquisition, and further precisely adjusted by measurements of overlap using image analysis software (IPLab Spectrum, version 3.6.5, BD Biosciences, Inc., Rockville, Maryland). Based on our experience, the overlap between images remained repeatedly consistent across large mosaics with minimal errors. After cropping, the images were concatenated into a single composite mosaic. The cropping removes the dark bands due to field curvature. The illumination falloff due to vignetting was then corrected for with inverted-brightness correction polynomial fits in both

$x$  and  $y$  directions. The polynomials were empirically designed to flatten the illumination falloff across images. The design of the polynomials is specific to our fluorescence mosaics but is based on a destripe filter that was originally authored by Marc Lehman and is available as open-source software called GNU Image Manipulation Program (GIMP). Lehman's executable and source code can be downloaded at [www.GIMP.org](http://www.GIMP.org).

The pixel gray scale or brightness is defined as  $I(x, y)$ , where  $x$  and  $y$  are column and row positions, respectively, of individual pixels. Horizontally across the entire mosaic, the mean brightness profile  $\bar{I}(x)$  is determined by averaging pixel values in columns as a function of  $x$ -pixel location. Similarly, vertically across the entire mosaic, the mean brightness profile  $\bar{I}(y)$  is determined by averaging pixel values in each row as a function of  $y$ -pixel location. These are:

$$\bar{I}(x) = \sum_{y=1}^N I(x, y) / N, \quad (3)$$

where  $N$  is the total number of pixels (or rows) in each column,

$$\bar{I}(y) = \sum_{x=1}^M I(x, y) / M, \quad (4)$$

where  $M$  is the total number of pixels (or columns) in each row.

Averaging across columns and rows of the entire mosaics provides a globally smoothed low-frequency estimate of the spatial high-frequency variations in fluorescence from the tissue. The mean brightness profiles in Eqs. (3) and (4) represent both the fluorescence signal from the central regions of the images and the illumination falloff at the edges. Polynomial fits for brightness in the  $x$  direction and the  $y$  direction are further modeled in terms of a rolling average of the mean brightness profiles:

$$\bar{I}_{\text{rolling average}}(x) = \sum_{i=-W/2}^{W/2} \bar{I}(x+i) / W, \quad (5)$$

$$\bar{I}_{\text{rolling average}}(y) = \sum_{i=-W/2}^{W/2} \bar{I}(y+i) / W. \quad (6)$$

In Eqs. (5) and (6), the rolling average-based polynomial fits are locally smoothed versions of the mean brightness profiles. The rolling average polynomial fits, too, represent both the fluorescence signals from the central regions and the illumination falloff near the edges of the images. As will be evident from further equations later, the purpose of these polynomial fits is to spatially isolate the regions of low-frequency illumination falloff near the edges of the images from the relatively high-frequency fluorescence signals in the central regions. Isolating the two regions subsequently allows corrections to be applied mainly to the illumination falloff, but none to the fluorescence signals. The parameter  $W$  is the window width of a rolling average

filter. The width of the filter  $W$  was empirically tested in the range of 24 to 100 pixels. On the basis of visual examination, a small width of 36 pixels was found to provide the optimum match of the rolling average polynomial fit to the mean brightness profile. Smaller windows produced too little smoothing of the differences between the spatially high-frequency fluorescence signals in the central regions of the images and the relatively low-frequency illumination falloff near the edges, and therefore provided inadequate isolation of the two regions. This resulted in (unwanted but) minimal corrections to the fluorescence signal but too little correction for illumination falloff. Larger windows resulted in too much smoothing and, again, inadequate isolation, which resulted in too much correction of illumination falloff and also unwanted large corrections to the fluorescence signal.

Subtracting the mean brightness profiles from rolling average polynomial fits substantially removes the fluorescence signals from the central regions and mainly represents the illumination falloff near the edges. This subtraction results in an inverted-brightness correction polynomial that is determined to be:

$$C(x) = \bar{I}_{\text{rolling average}}(x) - \bar{I}(x), \quad (7)$$

$$C(y) = \bar{I}_{\text{rolling average}}(y) - \bar{I}(y). \quad (8)$$

The correction polynomials  $C(x)$  and  $C(y)$  are minimal in the central regions of images of the mosaic, which are relatively uniformly illuminated. Visual examination showed that, with the rolling average filter width of 36 pixels, the correction polynomials were close to zero. However, they were appropriately large near the edges that display illumination falloff. Thus, the correction polynomials are applied mainly in the regions of illumination falloff but not in the central regions of images.

The inverted-brightness correction polynomials are added back to the original mosaic to flatten the illumination falloff across the images. The illumination falloff at the edges between images are corrected in the  $y$  direction (row by row) and in the  $x$  direction (column by column) to produce a new brightness or pixel grayscale distribution defined by:

$$I_{\text{new}}(x,y) = I(x,y) + [C(x)/D] \times \sum_{i=-W/2}^{W/2} I(x+i,y)/W, \quad (9)$$

$$I_{\text{new}}(x,y) = I(x,y) + [C(y)/D] \times \sum_{i=-W/2}^{W/2} I(x,y+i)/W. \quad (10)$$

In Eqs. (9) and (10),  $W$  is the width of rolling average filter (as before), and  $D$  is a scaling factor or “gain” for image brightness. Since the corrections are based on a rolling average approximation of the actual pixel brightness distribution, a scaling factor is necessary to adjust the brightness in the regions of fluorescence signal and vignetting to appropriate levels. The scaling factor  $D$  was empirically tested in the range of 8 to 128. On the basis of visual examination, a factor of 32 was determined to provide the optimum brightness for the mosaics.

Smaller scaling factors result in dark-appearing mosaics, whereas larger scaling factors result in too much brightness and saturation. To every row (or column) of pixel gray scales  $I(x, y)$ , the inverted-brightness polynomial fits are applied proportionally to the locally averaged fluorescence signal, as described in Eqs. (9) and (10). This approach minimizes the unnecessary corrections in relatively uniformly illuminated central regions of images and limits corrections mainly to the illumination falloff near the edges.

Based on our experience, this algorithm works effectively to correct the well-defined loss of illumination at the edges of images due to vignetting. The algorithm was applied to the 50 mosaics that were acquired to achieve repeatable results. The advantage of this algorithm is that the correction polynomials may be determined in a “blinded” manner to any given mosaic without requiring *a priori* knowledge of vignetting in the microscope. The mean brightness profiles and rolling average polynomial fits [Eqs. (3)–(6)] produce an estimate of the illumination falloff due to vignetting. Any additional instrumental errors in illumination are also estimated and corrected for. (An alternative is to directly fit polynomials based on instrument calibrations such as shown in Fig. 2. This may require frequent alignment and measurements of the microscope—a task that is easily performed in laboratory settings but not always in a clinical setting.) The main requirement is that values for  $W$  and  $D$  must be initially determined in two to three mosaics. We have found that the values may be consistently used afterwards. The disadvantage of this algorithm, however, is unwarranted decrease or increase of contrast in tissue morphologic features, especially at the edges of BCC tumors, due to the unnecessary corrections produced by the smoothing effect of the rolling average model. However, the corrections are close to zero in the fluorescence signal such that visual gain or loss of contrast appeared to be minimal and did not appear to affect subsequent analysis of mosaics and comparison to histology. The final processed mosaic is saved in TIFF format. (The algorithm and MATLAB software, including implementation details, are available to researchers who may be interested.)

## 2.8 Display of Large-Area Mosaics

Each image consists of  $640 \times 480$  pixels, is 8-bit gray scale, and requires about 1/4 MB of memory. Thus, a full mosaic of up to  $36 \times 36$  images consists of  $23,040 \times 17,280$  pixels and requires 325 MB of memory. The mosaics are scaled down using bilinear interpolation to make the displayed lateral resolution and pixelation equivalent to that of a  $2\times$ -magnified view of histology. The scaling down of the optical resolution and pixelation to match that of a  $2\times$  view was explained in detail in our earlier report on reflectance mosaicing.<sup>4</sup> The final mosaic is displayed to the Mohs surgeon with lateral resolution of  $\sim 4$  mm, consists of  $\sim 2500 \times 2500$  pixels, and requires less than 4 MB.

Mohs excisions are sometimes oval or elongated in shape and may be as long as 30 mm. For such excisions, larger mosaics displaying up to  $30 \times 10$  mm were created by acquiring multiple adjacent  $10 \times 10$  mm mosaics and joining them in Adobe Photoshop.

We observe mosaics on a 30-in. flat-screen monitor (Dell 222-7175 with a GeForce 8800 GTS video card) of  $2500 \times 1600$  pixels. A full-size mosaic is equivalent to a  $2\times$ -magnified view. With digital zooming, smaller portions, called submosaics, are also observed. The display of submosaics is equivalent to higher magnifications of  $4\times$  and  $10\times$ .

## 2.9 Comparison of Mosaics to Frozen Histology

Fifty mosaics were compared to the corresponding Mohs frozen histology sections. The frozen sections were those that were prepared during surgery for the Mohs surgeon. These sections were prepared with standard hematoxylin-and-eosin (H&E) stains. The imaged surface of the

frozen-thawed discarded excision corresponds to the final section that was prepared. Therefore, mosaics were compared to the last Mohs frozen section.

Nuclear and morphological features were evaluated in the mosaics and compared to the histology. The Mohs surgeon evaluated those features that are routinely examined in histology and are necessary to detect BCC tumors versus normal skin. The features for the presence of BCC tumors are nuclear pleomorphism (atypical shapes and sizes), increased overall nuclear density, palisading (“picket-fence” type arrangement of nuclei around the inner periphery of tumor), clefting (dark-appearing “moats” around the outer periphery of tumors that are filled with optically clear mucin), and the presence of inflammatory infiltrates. The features for normal skin are epidermal margin (epidermis along half the periphery of the excision), hair follicles, sebaceous glands, and eccrine glands.

The Mohs surgeon uses an objective lens with 2× magnification to quickly examine large areas of histology. Objective lenses with 4× and 10× magnifications are used, when necessary, for closer inspection of nuclear detail. Entire mosaics and submosaics were evaluated at equivalent magnifications. The submosaics usually consisted of a quarter of the entire mosaic, since the Mohs surgeon usually records the presence or absence of BCC tumor in quadrants.

### **2.10 Effects of Acridine Orange Staining on Subsequent Frozen Histology**

Experiments were performed to investigate the effects of exposure for 20 s to 1 mM acridine orange on subsequent histology. Possible effects include tissue decay, degradation of RNA and DNA due to autolysis, room-temperature digestion of tissue due to proteolytic enzymes, swelling of cytoplasm, and separation of the epidermis from the dermis. These effects may lead to prevention of H&E staining and a “washed out” appearance. Ten excisions were reprocessed for frozen H&E-stained histology sections after acridine orange staining and confocal imaging. The frozen sections were compared to the corresponding Mohs sections. The evaluation and comparison, performed under “blinded” conditions by the Mohs surgeon, analyzed possible tissue disruptions and distortions as well as the chromaticity of staining.

## **3 Results**

### **3.1 Mosaicing Enables Rapid Examination of Surgical Excisions**

Figures 3–5 show mosaics with significantly improved contrast, compared to those from our earlier studies. The 50 mosaics that were created, for comparison to histology, demonstrate repeatability of the tissue fixturing and mosaicing algorithm. Lateral registration between the edges of images was observed to be subpixel. The mosaics appear reasonably seamless and contiguous with high resolution and reasonably uniform illumination over large areas of tissue and are useful for clinical visualization and comparison to histology. The image quality of the mosaics is repeatable and consistently high for examination of morphologic features that are clinically important for surgical pathology. In Mohs skin excisions, the features include the edges of the tissue, epidermal margins, normal dermis, and nuclear detail and gross morphology of BCCs.

### **3.2 Confocal Mosaics Compare Well to Frozen Histology for All Types of BCCs: Demonstrates Detectability of Both Large and Small Tumors**

Excellent comparison between confocal mosaics and the corresponding Mohs frozen histology was achieved for BCCs as well as normal skin morphology. The epidermal margin of excisions along with the dermo-epidermal junction is clearly and repeatably identified on the mosaics. Normal structures in the dermis such as sebaceous glands, hair follicles, and eccrine glands are easily and consistently visualized. The gross morphology of BCCs in terms of shape, size, and location of tumor nests as seen in the mosaics corresponds well to that seen in frozen histology.

Additionally, the atypical morphology of nuclei in BCCs in terms of pleomorphism (varying shapes, sizes, orientations, and irregular distributions), crowding (increased density), and palisading is clearly visualized in the mosaics and corresponds well to the histology. Inflammatory infiltrates are seen around BCC nests. Nuclear staining with acridine orange clearly provided enhanced fluorescence contrast of tumors over the background dermis for both large and small types of BCCs. The large types include superficial and nodular, while the small types include micronodular, infiltrative, and sclerosing. Since the large types are easily detectable (including with reflectance contrast), we present the more challenging cases of small types in Figs. 3–5.

Figure 3 is a 2 $\times$ -view mosaic of a micronodular BCC and the corresponding histology. The overall tissue is disrupted by small tumors. Such tissue disruption is a gross feature that is usually intuitively identified by the Mohs surgeon. Small nests or nodules of tumor containing bright nuclei are seen in the mosaic, similar to those seen in the histology in terms of location and extent. The “tumor burden,” meaning extent of area occupied by tumor relative to the total appears approximately the same in both. Inflammatory cells around the tumors are also seen. The peripheral edges of the excision are completely delineated all along the excision. Along the top-and-left half portion of the periphery, we see the epidermis with bright but normal nuclei and also the dermo-epidermal junction. (Accurate and consistent detection of epidermis along half the tissue periphery is a must for Mohs pathology.) Other normal features include hair follicles and sebaceous glands, also with normal nuclei. The features are labeled and better appreciated in Fig. 4.

The mosaic shows the ability of acridine orange to provide strong contrast. Close examination, however, of the top-left quadrant of the mosaic reveals residual artifacts of dark bands due to field curvature. The presence of bands reveals the incomplete correction that may happen when the mosaics are acquired at a too-shallow depth below the glass window to tissue surface (for reasons that were explained earlier). The nuclear and morphologic detail and overall mosaic quality appears far superior on our large monitor than that that may be appreciated in small-size printed displays on paper. To display the detail that we routinely observe, a small portion of the mosaic is shown in Fig. 4.

Figure 4 is a submosaic with magnification of 6 $\times$  that displays a small region of the mosaic in Fig. 3, along with the corresponding histology. The high-magnification view in Fig. 4 illustrates morphology in detail compared to the low-magnification view in Fig. 3, which illustrates overall correlation to histology. Details of observed micronodular BCC morphology are described in the figure caption. The tumors often appear somewhat brighter than normal features due to the increased nuclear density and increased nuclear-to-cytoplasm ratio.

Figure 5 shows a 2 $\times$ -view mosaic and a 4 $\times$ -view submosaic that display the smaller infiltrative-type BCC tumors in the deeper dermis. Infiltrative BCCs were seen in 20% of the excisions. Thin strands of tumor were detectable in every case in 2 $\times$  views or in some cases with slightly higher magnification of 4 $\times$ . (Infiltrative BCCs had proven undetectable in previous reflectance contrast because they had shape and brightness similar to surrounding collagen fibers and bundles.) Figure 5 is an example of the most challenging cases. Various normal nucleated features in the dermis such as hair follicles, sebaceous glands, glandular cells, and inflammatory cells uptake acridine orange, which then results in substantial background brightness. Therefore, infiltrative tumor strands that are one cell thin are more difficult to detect.

Figure 6 is a 10 $\times$ -view submosaic that displays infiltrative-type BCC tumor at higher magnification and the corresponding histology. The contiguity of the thin tumor strands allows visual differentiation from the surrounding discrete distribution of inflammatory cells. The

challenge for detecting such thin tumor strands within inflammatory cells in confocal mosaics is similar to that in histology.

The results clearly show that magnification is important for tumor detection. As an extreme example, detection of the smallest and thinnest tumors is always possible in individual images at 30× magnification. However, for confocal mosaics, 2× magnification supplemented with, whenever necessary, slightly higher 4× magnification proved to be adequate. In Fig. 3, the micronodular tumors are surrounded by relatively sparse inflammatory cells and hence detectable in the 2× view. By comparison, in Fig. 5, the infiltrative BCC tumors are surrounded by dense inflammatory cells and hence required a 4× view to detect. At 4× magnification, normal structures could be easily differentiated from micronodules and thin strands of tumor. Thus, with 2× to 4× magnifications, mosaics were confidently evaluated for both presence and absence of tumors. When the display magnification increases from 2× to 4×, the resolution improves from ~4  $\mu\text{m}$  to ~2  $\mu\text{m}$ .

### 3.3 Acridine Orange Staining Does Not Affect Subsequent Frozen Histology

The effect of acridine orange staining and confocal mosaicing on subsequent tissue processing and H&E-stained frozen histology was minimal. There was no difference in the staining of the nuclear, cellular, and dermal morphology between the frozen sections that were prepared before and after imaging. The acridine orange-staining process does not alter the tissue in any way and does not adversely affect the ability of subsequent H&E-stained frozen sections to deliver accurate clinical diagnoses. However, there was minor tissue degradation in two (out of ten) excisions. The frozen sections that were prepared after imaging indicated disrupted tissue and inefficient H&E-staining compared to the ones before. Over the course of ten excisions that were reprocessed, we realized that the prolonged exposure of the tissue to our relatively warm laboratory room temperature was causing tissue degradation. Care was then taken to keep the excisions cool in isotonic saline solution before and after imaging and to expedite the reprocessing. This subsequently led to reproducible frozen sections for the remaining eight excisions.

## 4 Conclusions and Discussion

Confocal mosaicing microscopy, with the use of contrast agents and specialized tissue fixturing, enables the rapid observation of large areas of surgically excised tissue. Creating mosaics requires up to 9 min at present, whereas preparation of frozen histology requires 20 to 45 min per excision.<sup>1,4</sup> The use of fluorescence (instead of reflectance) with acridine orange to increase nuclei-to-dermis contrast significantly improves the detectability of all types of tumors. Using 1 mM acridine orange solution with 20 s immersion increased the brightness and contrast of tumors significantly relative to the surrounding collagen in the dermis. Exposure to this concentration and short immersion time did not affect the compliance of the tissue or affect subsequent frozen histology, provided that the excisions were kept hydrated and cool and refrozen in less than 30 min. Comparison of mosaics to histology confirmed that large types of BCCs such as superficial and nodular as well as small types such as micronodular, infiltrative, and sclerosing are easily detected.

By displaying mosaics at 2× magnification and submosaics at 4×, the observations and limitations with confocal microscopy approach those with frozen histology. Detectability of BCCs in both mosaics and histology with 2× magnification is challenged by small tumors within dense inflammatory infiltrates. In the most difficult cases containing very small or tiny tumors, slightly higher magnification of 4× with better resolution proved adequate to clearly visualize nuclear and morphologic detail. Our conclusion is that 2× and 4× magnifications are sufficient for detection of all types of BCC tumors in acridine orange-stained fluorescence mosaics. Higher magnifications are not necessary. The results demonstrate the feasibility of

low-magnification, large-area confocal mosaicing microscopy toward rapid noninvasive surgical pathology to potentially expedite and guide Mohs surgery. With further advances, this technology may find applications in diverse surgical settings.

A key requirement will be development of both exogenous and endogenous sources of contrast for diverse types of tissues. Instead of a single mode, two or more modes of contrast (i.e., multimodal contrast) may prove to be more effective: a “positive” mode for detecting the presence of tumor and a “negative” mode for detecting the absence of tumor (i.e., presence of normal tissue). This would be similar to the use of positive and negative stains in histology. Multimodal contrast is being investigated by several groups for imaging of BCCs. In particular, excellent correlation to histology was shown by Yaroslavsky's group, for all types of BCCs and SCCs, using methylene blue and toluidene blue, and combined fluorescence, reflectance, and fluorescence polarization modes.<sup>6</sup> Further development of such multimodal instruments is likely to improve sensitivity and specificity of detectability of tumors.

The mosaicing must be made faster to enable clinical studies, toward eventual acceptance by surgeons. Mosaics are created at present using one PC for acquisition and another networked PC for image-stitching, processing, and display. Rapid mosaicing will be obviously possible with the use of a single PC and real-time stitching in parallel with acquisition of images. Acquisition may be made faster with continuous capture of images that is synchronized to continuous stepping of the translation stages (instead of the current discrete and slow step-and-capture implementation). Preliminary analysis suggests that mosaics of  $20 \times 20$  mm may be created in about 2 to 3 min.

The quality of the mosaics may be improved with more seamless stitching of images and better correction for illumination falloff. Mosaics with perfectly (or near perfectly) seamless stitching of images is possible with lateral registration of images by matching features at the edges between images.<sup>13,14</sup> However, this will require additional processing time. Preliminary attempts based on cross-correlation on a desktop PC required  $\sim 10$  s for  $3 \times 3$  images, which scales up to  $\sim 20$  minutes for  $35 \times 35$  images. The processing time may be significantly reduced with a smaller number of images (using lower-magnification, lower-NA objective lenses with larger field of view) and faster computers. Since speed will be a key requirement in the surgical setting for performing real-time pathology-at-the-bedside, a compromise between image-stitching quality and processing time must be determined.

Mosaicing and detection of SCCs must also be investigated. Our initial studies have focused on BCCs since the incidence of SCCs is about 3 to 4 times less with, consequently, a much smaller number of Mohs surgical cases. Although detection of nuclei remains the key requirement, the additional examination of cellular cytoplasm for necrosis and keratinization is often important in the case of SCCs. Thus, multimodal contrast that specifically stains cellular cytoplasm may be necessary.

As with any new technology, “image understanding” and the ability to read mosaics will be a key factor for advancing toward clinical utility. Our experience with two Mohs surgeons suggests that the learning curve for reading confocal mosaics will be fairly rapid for those familiar with Mohs histology. Mosaics must be quantitatively validated against histology for sensitivity and specificity for both positive (i.e., presence of BCCs) and negative (i.e., absence of BCCs). A preclinical study is presently in progress by two Mohs surgeons who are performing a blind evaluation of the fifty mosaics and a statistical correlation to histology to determine sensitivity and specificity. The study will be followed by clinical trials directly on fresh excisions at the bedside during Mohs surgery.

Although the only excisions imaged were from Mohs surgery of skin cancer, large-area mosaicing may prove useful to interrogate other excisions such as of oral mucosa, thyroid nodules, parathyroid glands, and bone during head-and-neck surgery, needle core-biopsies and lumpectomies of breast, and intraoperative biopsies of liver, bladder, and other tissues. In the long term, confocal mosaicing microscopy may evolve into either an adjunct or, possibly, an entirely new alternative to frozen histology to guide surgery in real time in many settings with high-impact, high-value outcomes without the time delays, limitations, or high costs of today's histology procedures.

## Acknowledgements

The authors thank Mohs histology technicians Marie Tudisco and Barbara Strippoli for supplying discarded excisions, help with the frozen histology, and their intellectual involvement with all aspects of this research. The authors are grateful to Jay Eastman and William Fox of Lucid, Inc., for technical support. This research was funded partly by NIH Grant No. R01EB002715 from the Image-Guided Interventions program of the NIBIB (Program Officer Dr. John Haller) and partly by a grant from the Byrne Fund, Department of Medicine at MSKCC.

## References

1. Rajadhyaksha M, Menaker G, Flotte TJ, Dwyer PJ, Gonzalez S. Rapid confocal examination of nonmelanoma cancers in skin excisions to potentially guide Mohs micrographic surgery. *J Invest Dermatol* 2001;117:1137–1143. [PubMed: 11710924]
2. Bialy TL, Whalen J, Veledar E, Lafreniere D, Spiro J, Chartier T, Chen SC. Mohs micrographic surgery versus traditional surgical excision—a cost comparison analysis. *Arch Dermatol* 2004;140:736–742. [PubMed: 15210467]
3. Chung VQ, Dwyer PJ, Nehal KS, Rajadhyaksha M, Menaker GM, Charles C, Jiang SB. Use of *ex vivo* confocal scanning laser microscopy during Mohs surgery for nonmelanoma skin cancers. *Dermatol Surg* 2004;30:1470–1478. [PubMed: 15606734]
4. Patel YG, Nehal KS, Aranda I, Li Y, Halpern AC, Rajadhyaksha M. Confocal reflectance mosaicing of basal cell carcinomas in Mohs surgical skin excisions. *J Biomed Opt* 2007;12(3):034027. [PubMed: 17614735]
5. Rajadhyaksha M, Gonzalez S, Zavislan JM. Detectability of contrast agents for confocal reflectance imaging of skin and microcirculation. *J Biomed Opt* 2004;9:323–331. [PubMed: 15065898]
6. Al-Arashi M, Salomatina E, Yaroslavsky AN. Multimodal confocal microscopy for diagnosing nonmelanoma skin cancers. *Lasers Surg Med* 2007;39:696–705. [PubMed: 17960751]
7. Rouse AR, Gmitro AF. Multispectral imaging with a confocal microendoscope. *Opt Lett* 2000;25(23):1708–1710. [PubMed: 18066321]
8. Darzynkiewicz, Z. Differential staining of DNA and RNA in intact cells and isolated cell nuclei with acridine orange, Chapter 27. In: Darzynkiewicz, Z.; Crissman, HA., editors. *Methods in Cell biology*. Vol. 33. Academic Press; New York: 1990. p. 285-298.
9. Kubota Y, Steiner RF. Fluorescence decay and quantum yield characteristics of acridine orange and proflavine bound to DNA. *Biophys Chem* 1977;6:279–289. [PubMed: 880342]
10. Rajadhyaksha, M.; Gonzalez, S. Real-time *in vivo* confocal fluorescence microscopy, Chapter 5. In: Mycek, MA.; Pogue, B., editors. *Handbook of Biomedical Fluorescence*. Marcel-Dekker; New York: 2003. p. 143-180.
11. Cuccia DJ, Bevilacqua F, Durkin AJ, Merritt S, Tromberg BJ, Gulsen G, Yu H, Wang J, Nalcioğlu O. *In vivo* quantification of optical contrast agent dynamics in rat tumors by use of diffuse optical spectroscopy and magnetic resonance imaging. *Appl Opt* 2003;42(16):2940–2950. [PubMed: 12790443]
12. Nugent LJ, Jain RK. Extravascular diffusion in normal and neoplastic tissues. *Cancer Res* 1984;44:238–244. [PubMed: 6197161]
13. Chow SK, Hakozaiki H, Price DL, Maclean NAB, Deernick TJ, Bouwer JC, Martone ME, Peletier ST, Ellisman MH. Automated microscopy system for mosaic acquisition and processing. *J Microsc* 2006;222(2):76–84. [PubMed: 16774516]

14. Sun C, Beare R, Volker H, Jackway P. Mosaicing of microscope images with global and radiometric corrections. *J Microsc* 2006;224(2):158–165. [PubMed: 17204063]

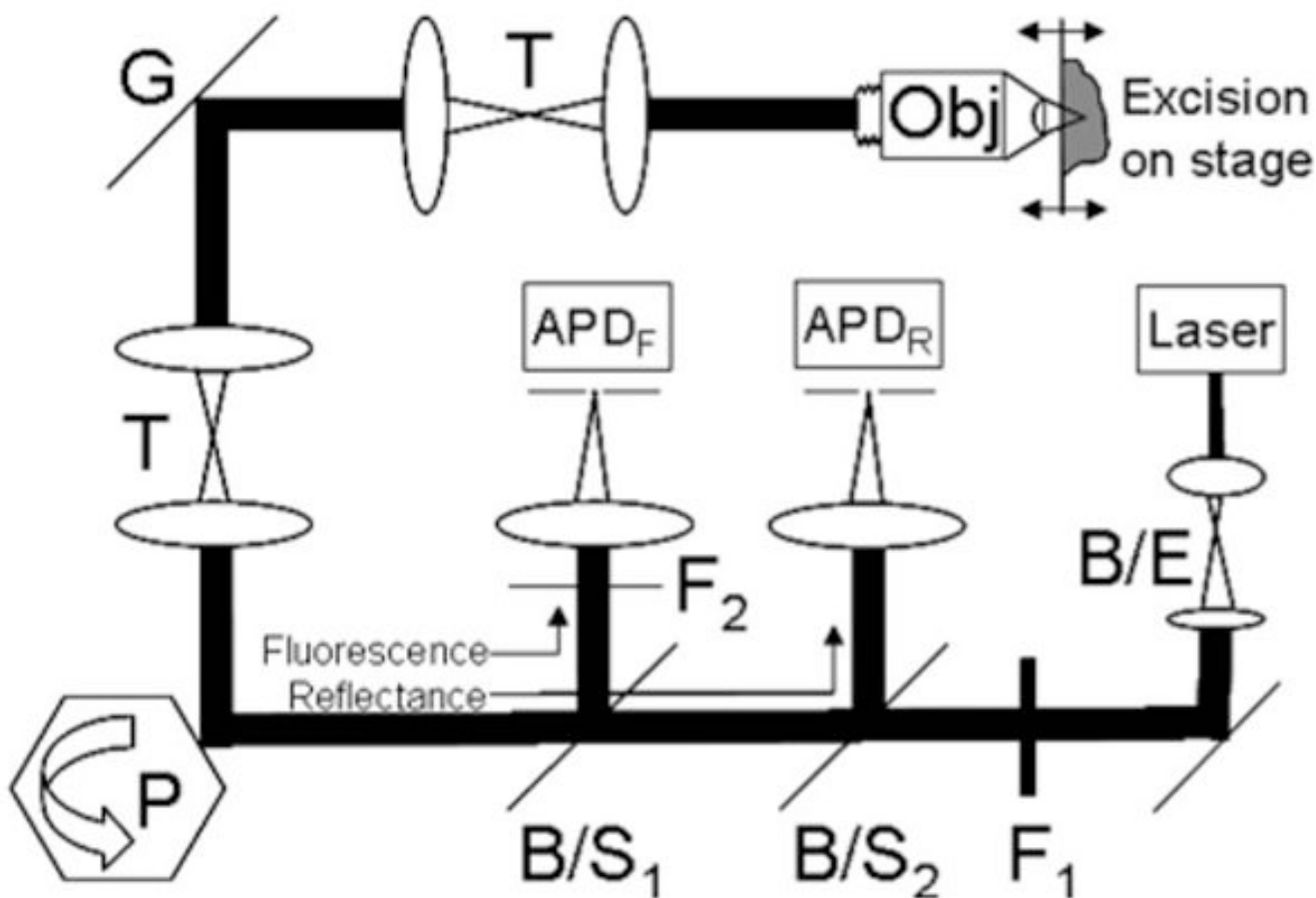


**Fig. 1.**

Optical design of the confocal microscope with the following components: argon-ion laser, 7× beam expander (B/E), 488-nm-excitation selection filter ( $F_1$ ), spinning polygon (P), galvanometric scan mirror (G), relay telescopes (T), and objective lens (Obj). A dichroic beamsplitter ( $B/S_1$ ) steers fluorescent emission toward an avalanche photodiode ( $APD_F$ ) through the 488-nm-rejection filter ( $F_2$ ). A polarizing beamsplitter ( $B/S_2$ ) steers reflected light toward another avalanche photodiode ( $APD_R$ ).

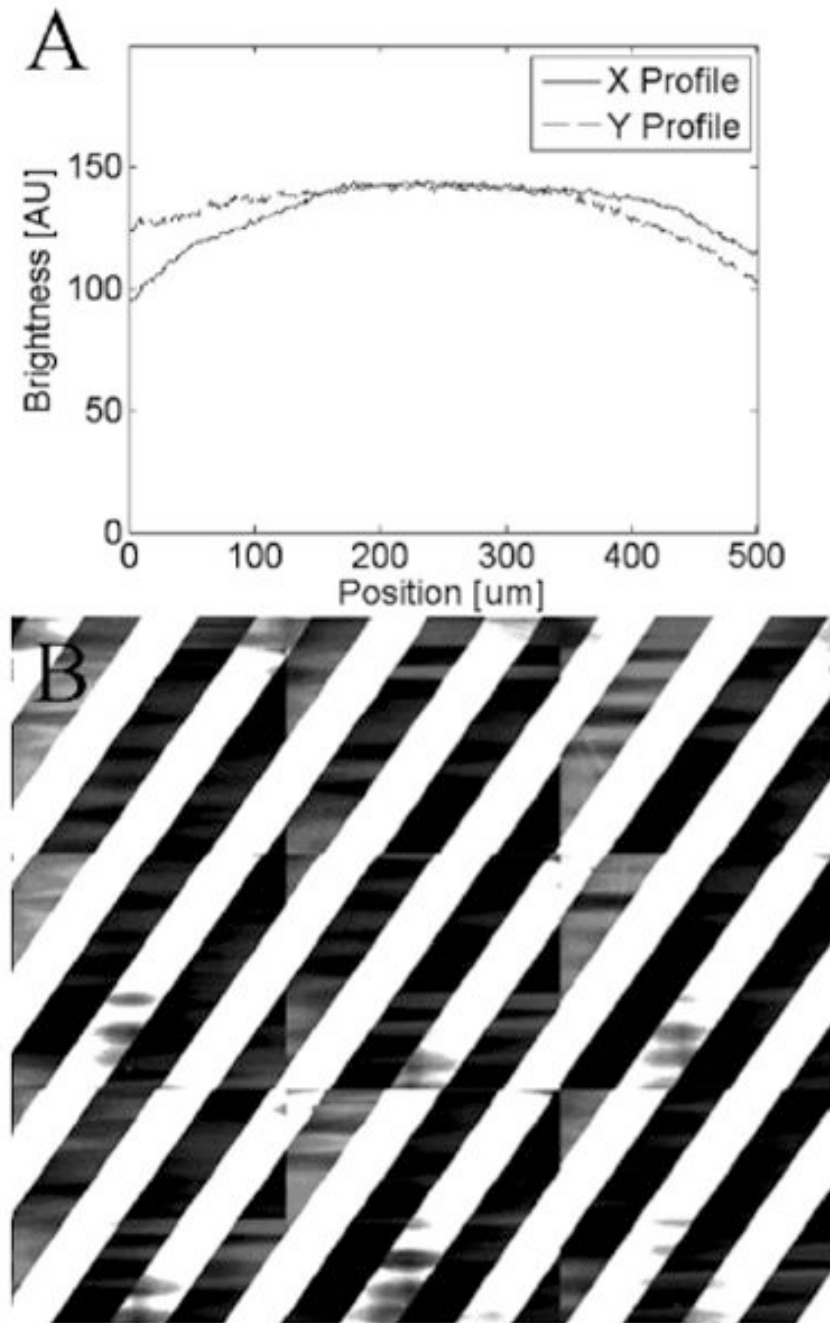


**Fig. 2.** Calibration measurements showing: (a) illumination falloff due to vignetting in the  $x$  and  $y$  directions across the field of view, and (b)  $3 \times 3$  mosaic of a reflective grating target indicating angular alignment and lateral registration to within five pixels (which scales down to subpixel in the final mosaics).

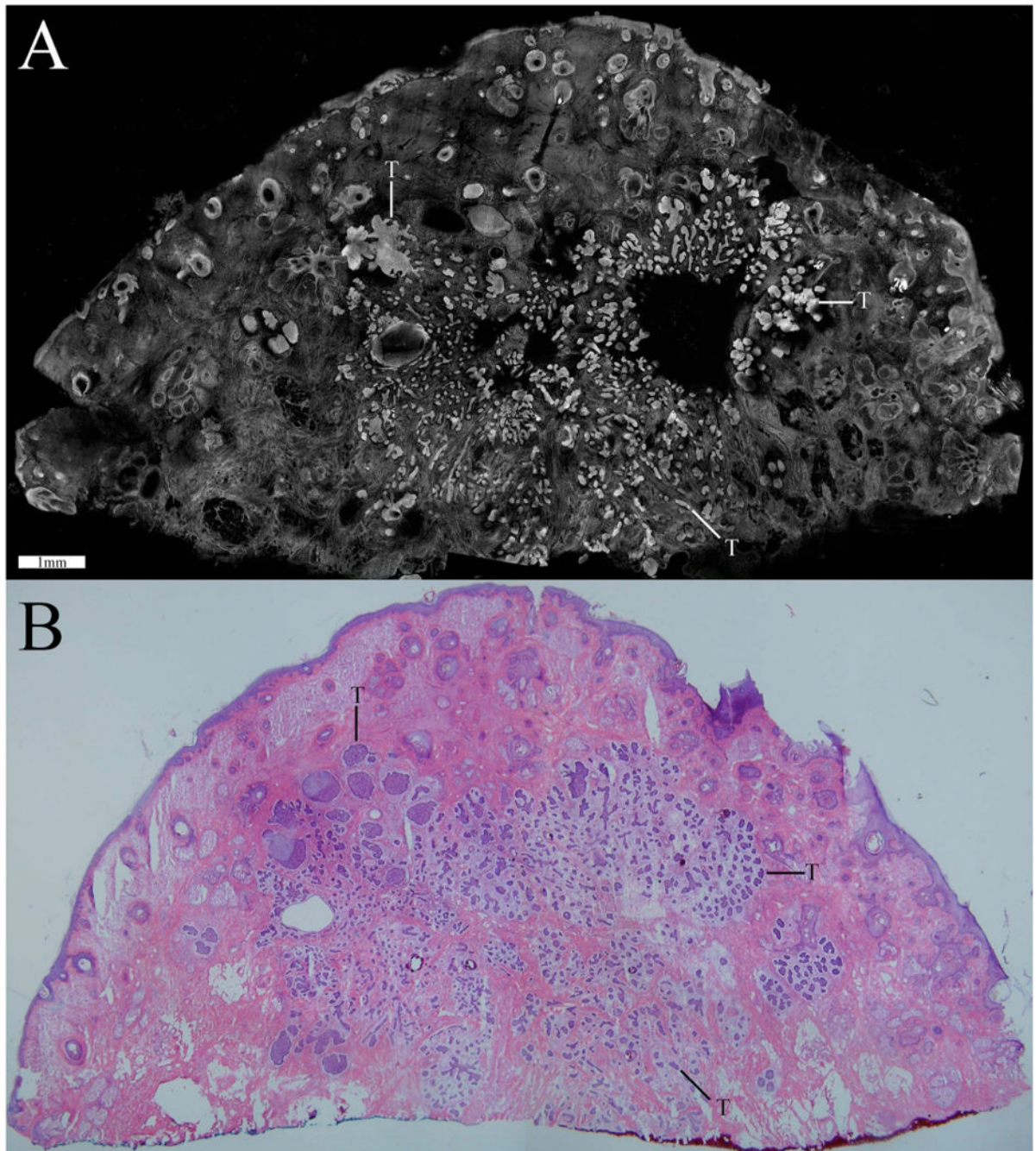


**Fig. 3.** Confocal mosaic (a) of a micronodular BCC that compares well to the corresponding histology (b). Small and tiny nodules or nests of tumor are seen (T) appearing bright in the mosaic and purple-stained in the histology. (Color online only.)

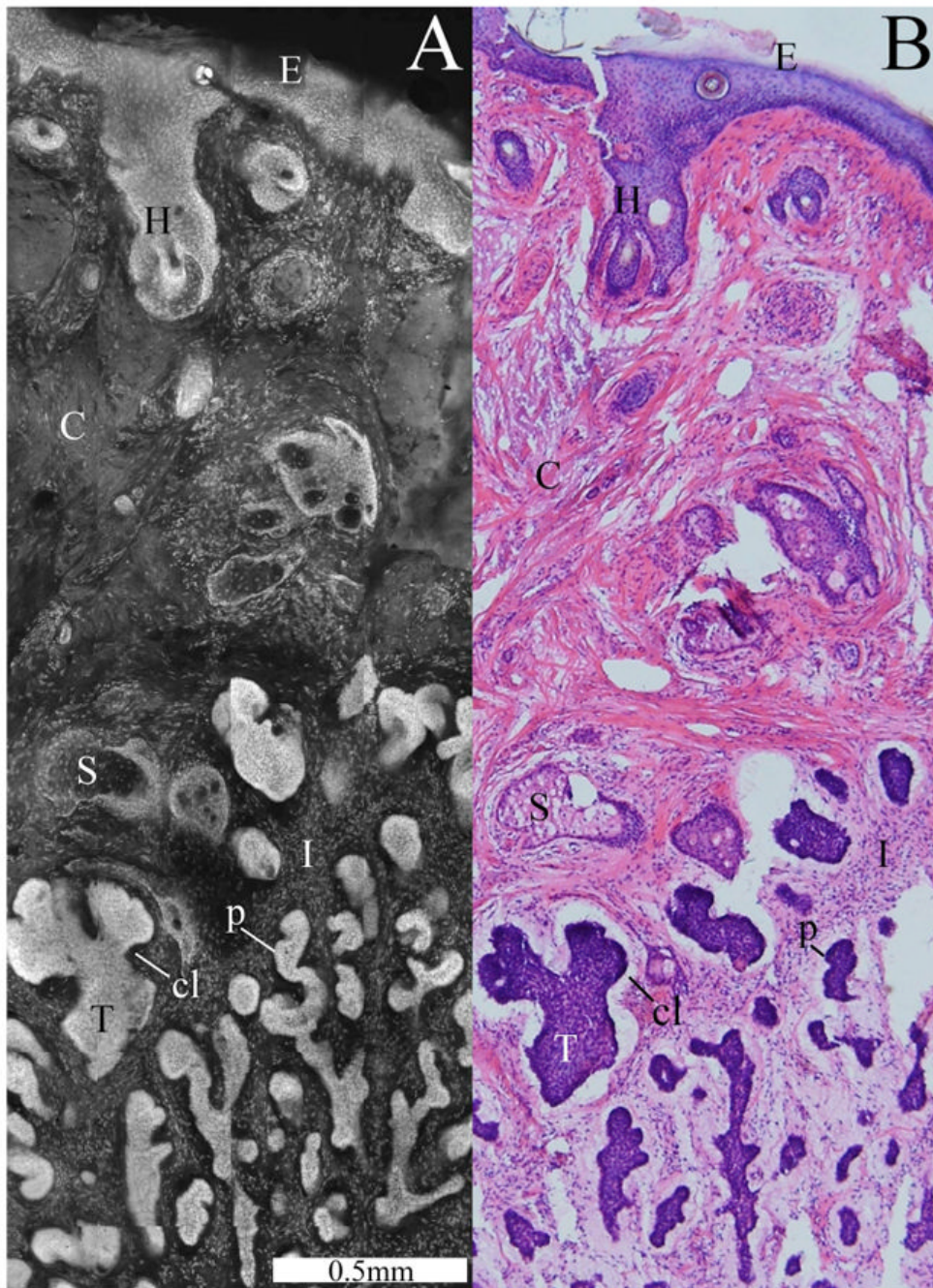


**Fig. 4.** Confocal submosaic (a) showing a magnified 6 $\times$  view of the mosaic in Fig. 3 and comparable histology (b). A micronodular BCC tumor (T) is seen with features such as nuclear pleomorphism, increased nuclear density, palisading (p), and clefting (cl). Normal features are seen such as the epidermis (E), a hair follicle (H), sebaceous glands (S), dermal collagen (C), and inflammatory cells (I).

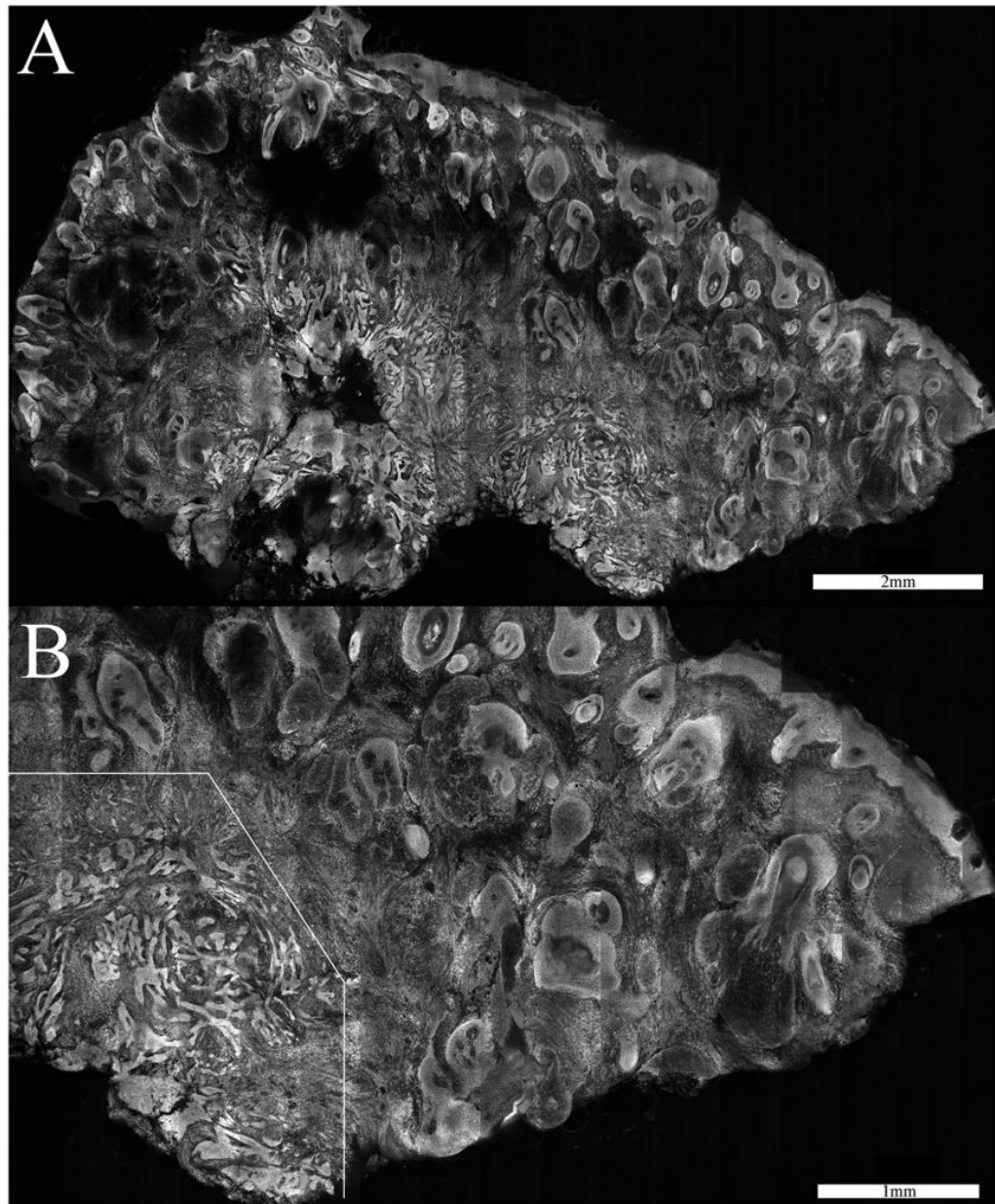


**Fig. 5.** Confocal mosaic (a) of an infiltrative BCC. Thin strands of tumor lie in the deeper dermis. The tumor is not clearly visualized in the 2 $\times$  view but is more obvious in the slightly magnified 4 $\times$  view (b). The overall disruption of the tissue is evident in the lower-left portion.

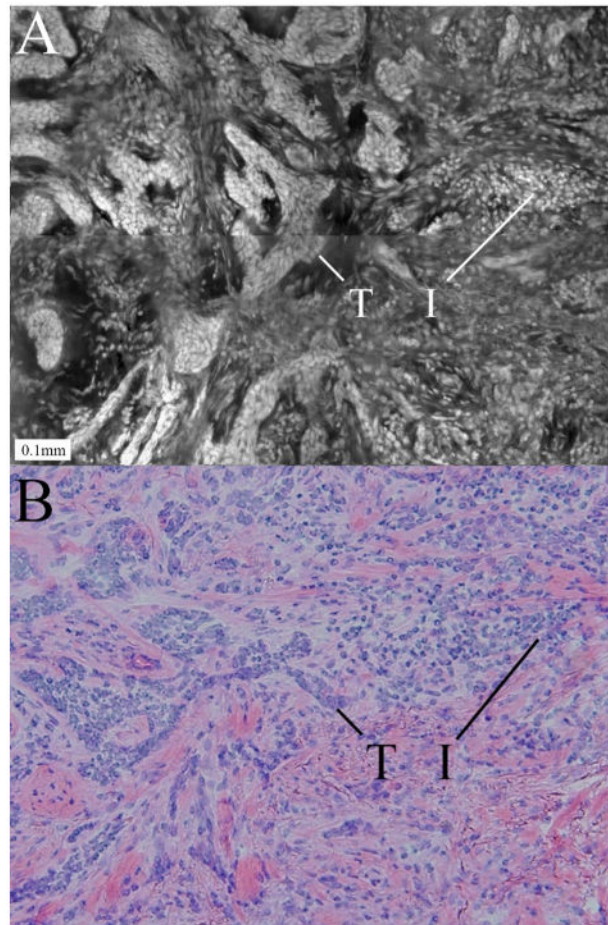


**Fig. 6.** Confocal submosaic (a) showing a higher magnification 10× view of the mosaic in Fig. 5 and comparable histology (b). Both images show infiltrative BCC tumor (T) surrounded by inflammatory infiltrates (I). The contiguity of the thin tumor strands differentiates them from the surrounding discrete inflammatory cells. The challenge in detecting such thin tumor strands within inflammatory cells in mosaics is similar to that in histology.